Journal of Engineering in Industrial Research

2025, Volume 6, Issue 2

Original Research Article

Impact of Organic/Hole Transport Layer in Efficiency Optimization of $SnO_2/CH_3NH_3PbI_3$/Org/HTL Perovskite Solar Cell: A Simulation Study

Avishek Roy[1], Mostefa Benhaliliba[2,*], Asma Rahimi[3]

[1]Department of Electronics, Vidyasagar College, 39 Sankar Ghosh Lane, Kolkata-700006, India
[2]Film Device Fabrication-Characterization and Application FDFCA Research Group USTOMB, 31130, Oran, Algeria
[3]Department of Chemical Engineering, Faculty of Engineering, University of Kurdistan, Sanandaj, 66177, Iran

Citation A. Roy, M. Benhaliliba, A. Rahimi. Impact of organic/Hole Transport Layer in Efficiency Optimization of $SnO_2/CH_3NH_3PbI_3$/Org/HTL Perovskite Solar Cell: A Simulation Study. *J. Eng. Ind. Res.* **2025**, 6(2):157-178.

https://doi.org/10.48309/JEIRES.2025.499899.1151

Article info:
Submitted: 2025-01-14
Revised: 2025-03-16
Accepted: 2025-04-13
ID: JEIRES-2501-1151

Keywords:
Perovskite solar cells; CuSCN and CuI; Hole transport layer; Bandgap of HTL; P_3HT and MEHPPV; SCAPS-1D.

ABSTRACT

In solar energy applications, $CH_3NH_3PbI_3$ has offered a breakthrough in perovskite solar cell (PSC) research with different hole transport layers (HTL) and electron transport layers (ETL). This investigation studies $CH_3NH_3PbI_3$ PSC with SnO_2 as ETL and CuSCN or CuI as HTL. P_3HT and MEHPPV as an organic layer (Org) are inserted between $CH_3NH_3PbI_3$ and HTL. A simulation study is carried out on four combinations of $SnO_2/CH_3NH_3PbI_3$/Org/HTL/Au PSCs using SCAPS-1D. The current-voltage characteristics and energy bandgap of all the PSCs are discussed. The $SnO_2/CH_3NH_3PbI_3/P_3HT$/CuSCN/Au is the best PSC with Voc of 1.159 V, Jsc of 25.359 mA/cm^2, fill factor of 76.99% and a promising higher efficiency of 22.63% than others. The photovoltaic parameters of $SnO_2/CH_3NH_3PbI_3$/Org/HTL/Au are analyzed by varying the temperature, the thickness of the organic layers, and the bandgap of both the organic and inorganic HTLs to optimize the efficiency. Capacitance-voltage (C-V) plots are generated at various frequencies for all the proposed PSCs. The simulation results present a promising approach for the future design of highly efficient and stable PSCs.

Introduction

In recent years, researchers have been working to improve the efficiency of perovskite solar cells (PSCs) by combining distinct perovskite layers with different electron transport layers (ETL) and hole transport layers (HTL) [1-3]. The power conversion efficiency (PCE) of solar cells based on organic-inorganic halide perovskites has recently increased, but they also display odd behavior including current-voltage hysteresis and a low-frequency huge dielectric response [4]. The best compounds known as methyl ammonium lead halides (MALHs) have a perovskite structure and the chemical formula

***Corresponding Author: Mostefa Benhaliliba** (mbenhaliliba@gmail.com)

$CH_3NH_3PbX_3$, where X can be I, Br, or Cl. They have potential use in solar cells [5], lasers, light-emitting diodes [6], photodetectors [7], radiation detectors, scintillates, magneto-optical data storage, hydrogen synthesis, and other technologies [8-10]. Organometal Halide Perovskites as Photovoltaic Cell Visible-Light Sensitizers have been reported [1]. CuSCN (copper (I) thiocyanate) is a cuprous thiocyanate. It is a white, air-stable solid utilized as a starting material for various thiocyanate salts. The use of CuSCN as a generic transparent anodic interlayer material in high-efficiency bulk-heterojunction organic photovoltaic (OPV) devices produced by solution is early reported [11]. A TiO_2/perovskite/ CuSCN heterojunction solar cell was previously fabricated by Murugadoss *et al.* [12]. Due to its distinctively large band gap of (>3.5 eV), CuSCN often exhibits intrinsic hole transporting properties and extremely high transparency over the UV-Vis/NIR region [13,14]. CuI is a wide bandgap p-type inexpensive semiconductor with a high degree of stability [15]. The photovoltaic performance of electrochemically produced CuSCN-CuI bilayer-based inverted perovskite solar cells is investigated earlier [16]. Both CuSCN and CuI can play an effective role as HTL in designing high efficiency PSCs. Organic/inorganic hybrid hetero-junctions combine the benefits of both organic and inorganic semiconductors, utilizing the superior electrical properties of these materials alongside their effective film-forming capabilities [17]. The development of these hybrid semiconductor heterojunctions presents opportunities for a new class of semiconductor devices, which hold significant promise for applications in low-cost flexible electronics, optoelectronics, and photovoltaics. Extensive research has been conducted on poly (3-hexylthiophene-2,5-diyl) (P_3HT) and poly [2-methoxy-5-(2-ethylhexyloxy)-1,4-phenylenevinylene] (MEHPPV) thin films, demonstrating their potential as solar cell materials [18,19]. These conjugated polymers exhibit remarkable characteristics such as a band gap within the visible spectrum, high electrical conductivity, and commendable chemical stability under standard conditions, as previously highlighted by Karimi *et al.* [3]. P3HT and MEHPPV are effective donor materials that improve the performance of solar cells [20]. Tin oxide (SnO_2) has gained significant attention as an essential n-type semiconductor ETL due to its excellent electron extraction properties and stability compared to titanium dioxide (TiO_2) ETL leading to higher power conversion efficiencies in PSCs [21]. In this work, $SnO_2/CH_3NH_3PbI_3$ is studied with CuSCN and CuI as HTL. It is very interesting to study if an organic layer (P_3HT and MEHPPV) can be added between $CH_3NH_3PbI_3$ and HTL. A combination of inorganic-organic serving as HTL can improve the overall performance of the solar cell. The photovoltaic behavior of four proposed perovskite solar cells is discussed viz. i) $SnO_2/CH_3NH_3PbI_3/P_3HT$/CuSCN, ii) $SnO_2/CH_3NH_3PbI_3/P_3HT$/CuI, and iii) $SnO_2/CH_3NH_3PbI_3$/MEHPPV/CuSCN and iv) $SnO_2/CH_3NH_3PbI_3$/MEHPPV/CuI. We investigated the photovoltaic properties by varying the inorganic hole transport layers (HTLs) CuSCN and CuI alongside the organic P_3HT and MEHPPV layers using Solar Cell Capacitance Simulator (SCAPS). A strategic choice of Au as the metal back contact owing to its high work function has been simulated and proposed to improve device performance [22]. The current-voltage (I-V) characteristics under illumination are conducted to extract critical photovoltaic parameters (Voc, Jsc) that are key to optimizing efficiency. Furthermore, we meticulously examine the effects of the band gap variations (both inorganic HTLs and organic layers), thickness of the organic layers, as well as the temperature impact on all four proposed perovskite solar cells (PSCs). The C-V characteristics are also plotted at different frequencies. To our knowledge, there are no existing reports on the properties of $SnO_2/CH_3NH_3PbI_3$/Org/HTL/Au configurations in perovskite solar cells. The insights gained from the interface between CuSCN or CuI with P_3HT or MEHPPV is invaluable for advancing future research in PSC fabrication.

Solar Cell Structure

The numerical study is performed by the SCAPS-1D software which is developed by Burgelman *et al.* from the University of Gent, Belgium [23,24]. The simulator has been employed to design and analyze the photovoltaic performance of the solar cell.

Table 1: The electrical parameters of the layers in the solar cell structure

Parameters	**Sn_2O [30,32]**	**$CH_3NH_3PbI_3$ [3,27,29,32]**	**CuSCN [2,24,32]**	**CuI [2,27,33]**	**P_3HT [20,31,32]**	**MEHPPV [3,20]**
Thickness (nm)	200	1000	100	100	100	100
Band-gap (eV)	3.6	1.5	3.49	2.98	2.0	2.2
Electron affinity	4.0	3.9	1.9	2.1	3.2	2.8
Dielectric permittivity (relative)	9.0	30	10	6.5	3.0	3.0
CB effective density of states ($1/cm^3$)	$2.2x10^{18}$	$2.2x10^{18}$	$1.7x10^{19}$	$2.8x10^{19}$	$1x10^{20}$	$2.5x10^{19}$
VB effective density of states ($1/cm^3$)	$1.8x10^{19}$	$1.9x10^{19}$	$2.5x10^{21}$	$1x10^{19}$	$1x10^{20}$	$2.5x10^{19}$
Electron mobility (cm^2/Vs)	100	3.0	0.0001	$1.7x10^{-4}$	$1x10^{-4}$	$5x10^{-5}$
Hole mobility (cm^2/Vs)	0.256	17	0.1	$2x10^{-4}$	$1x10^{-3}$	$2.5x10^{-4}$
Shallow uniform donor density ($1/cm^3$)	$1x10^{17}$	$1x10^{13}$	0	0	0	0
Shallow uniform acceptor density ($1/cm^3$)	0	0	$1x10^{18}$	$1x10^{18}$	$1x10^{16}$	$1x10^{15}$

The operational framework of the simulator is based on semiconductor equations, which entail Poisson's equation, transport equations, and continuity equations, all approached in a one-dimensional (1D) context [25,26]. The current-voltage characteristics of the solar cells are obtained under AM 1.5 solar spectrum at 100 mW/cm^2 light intensity and under operating temperature of 300 K. The absorption coefficient is used at 10^5 cm^{-1}. In device simulation, the perovskite solar cell is $CH_3NH_3PbI_3$ along with SnO_2 as the n-type an electron transport layer (ETL). An organic-inorganic combination of hole transporting layer (HTL) is used. CuSCN or CuI as inorganic and P_3HT or MEHPPV as organic layer is considered. The holes are collected at the Au metal back contact. The electrical parameters for the various layers have been sourced from the recent publications that focus on optimizing efficiency. The parameters selected for each layer, which include mobility, bandgap, and electron affinity, are those that have demonstrated the highest efficiency to date. In this simulation, parameters have been chosen from multiple references to ensure the attainment of maximum efficiency [2,3,20,27-33]. The HTL, absorber perovskite and ETL thicknesses are defect-free layers. Table 1 lists the initial electrical device parameters of the different layers used as standard.

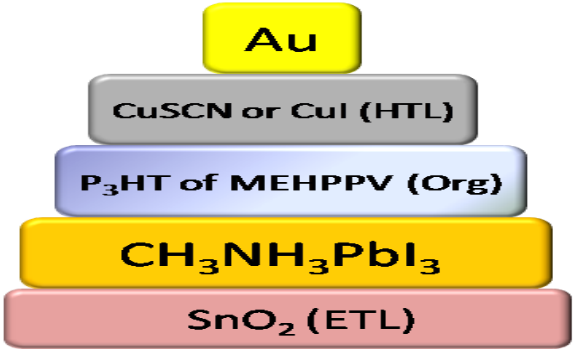

Figure 1: Schematic structure of $SnO_2/CH_3NH_3PbI_3$/Org/HTL/Au perovskite solar cell

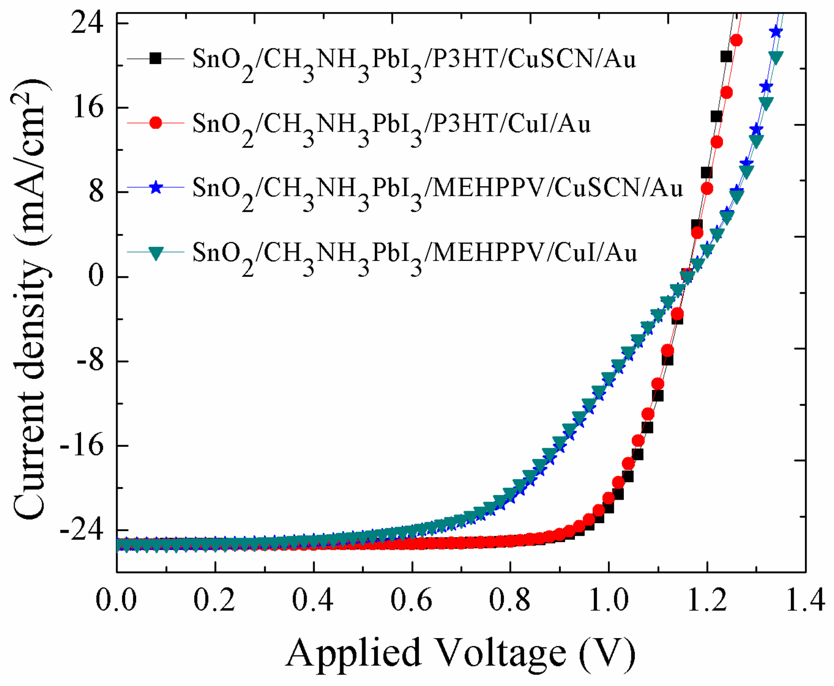

Figure 2: Current density – voltage (J-V) characteristics of the four different PSC. heterostructures.

Table 2: Photovoltaic parameters of the four perovskite solar cells

Perovskite solar cell	V_{OC} (V)	J_{SC} (mA/cm^2)	FF (%)	PCE (%)
$SnO_2/CH_3NH_3PbI_3/P_3HT/CuSCN/Au$	1.15906	25.35934	76.99	22.63
$SnO_2/CH_3NH_3PbI_3/P_3HT/CuI/Au$	1.15906	25.35907	75.64	22.23
$SnO_2/CH_3NH_3PbI_3/MEHPPV/CuSCN/Au$	1.15955	25.34007	57.21	16.81
$SnO_2/CH_3NH_3PbI_3/MEHPPV/CuI/Au$	1.15955	25.33777	56.33	16.55

Results and Discussion

J-V characteristics

Figure 1 describes the schematic structure of our methyl ammonium lead halides (MALH) perovskite solar cell.

Figure 2 depicts the current density versus applied voltage characteristics for four proposed perovskite solar cells (PSCs), with variations influenced by the hole transport layer (HTL) and organic layers incorporated. The non-linear plots associated with the $SnO_2/CH_3NH_3PbI_3/P_3HT/CuSCN/Au$ and $SnO_2/CH_3NH_3PbI_3/P_3HT/CuI/Au$ PSCs exhibit a more pronounced non-linear behavior compared to those for the $SnO_2/CH_3NH_3PbI_3/MEHPPV/CuSCN/Au$ and $SnO_2/CH_3NH_3PbI_3/MEHPPV/CuI/Au$ PSCs. The observed changes in current can be attributed to the integration of distinct organic layers within the PSC heterostructure. In the voltage range of 0.6 V to 1.1 V, the PSC utilizing MEHPPV demonstrates a greater current than that of the PSC utilizing the P_3HT organic layer. Conversely, this trend reverses within the 1.1 V to 1.4 V bias range, as P_3HT exhibits a higher current. The observed increase in reverse current, referred to as photocurrent, under illumination signifies the generation of charge carriers resulting from light absorption. This illumination occurs under standard AM 1.5 global spectral irradiance conditions. The influence of the organic and HTL layers on values of open circuit voltage (Voc), short circuit current density (Jsc), fill factor (FF), and power conversion efficiency (PCE) are provided in Table 2.

A comprehensive summary of the photovoltaic parameters derived from Figure 2 is provided in Table 2. The Voc for the P_3HT/CuSCN and

P_3HT/CuI PSCs is consistent at 1.15906 V, however, the Jsc is notably higher in the $P_3HT/CuSCN$ configuration. This results in an enhanced FF and PCE for the $SnO_2/CH_3NH_3PbI_3/P_3HT/CuSCN/Au$ PSC when compared to its $SnO_2/CH_3NH_3PbI_3/P_3HT/CuI/Au$ counterpart. Similarly, the Voc for the MEHPPV/CuSCN and MEHPPV/CuI PSCs also remains constant at 1.15955 V, yet the Jsc value is superior for the MEHPPV/CuSCN cell. This phenomenon contributes to an increased FF and PCE for the $SnO_2/CH_3NH_3PbI_3/MEHPPV/CuSCN/Au$ PSC relative to the $SnO_2/CH_3NH_3PbI3/MEHPPV/CuI/Au$ PSC. The enhancements in FF and Jsc can be ascribed to a reduction in surface recombination, which facilitates the improved movement of photo-induced minority carriers toward the opposing electrodes [34].

Among the four examined solar cells, the $SnO_2/CH_3NH_3PbI_3/P_3HT/CuSCN/Au$ solar cell achieves the highest power conversion efficiency at 22.63%. This fact reveals the use of the more efficient PSC based on $P_3HT/CuSCN$ layers. The wide bandgap of CuSCN compared to CuI helps in efficient collection of photons at the perovskite/HTL interface resulting more electron hole pair generation [35]. Previous literature has indicated that, in PSC heterostructures, the current-voltage (J-V) characteristics are recorded within a range of 0 to 1 V, achieving a current density of 20 mA/cm^2 for the FTO/bl-TiO_2/m-$TiO_2/CH_3NH_3PbI_3/CuSCN/Au$ PSC configuration utilizing CuSCN. In addition, the Voc values have been observed to range from 0.84 to 0.95 V, while the FF values remain closely aligned, reflective of the solvents utilized for CuSCN [12]. Moreover, as previously mentioned, the PDPP-2T-TT: PC 71 BM cells employing PEDOT: PSS and CuSCN as HTLs exhibit J-V curve characteristics similar to those observed in our PSC device [7]. The Jsc is recorded to vary from -18 mA/cm^2 to positive values within the biasing voltage range of -0.3 V to 0.9 V. Correspondingly, similar trends in J-V characteristics across the 0-0.8 V voltage range were reported by Mohanty *et al.* [36] for Al/PEDOT: $PSS/CH_3NH_3PbI_3/PCBM/FTO$ and $Al/CH_3NH_3PbI_3/PCBM/FTO$ solar cells. The reported PCE for PSCs utilizing PEDOT: PSS and PCBM are 17.23% and 15.23%, respectively [36]. Furthermore, through the experimental analysis of $CH_3NH_3PbI_3$ PSCs, Ghosh *et al.* reported J-V characteristics comparable to those observed in our study.

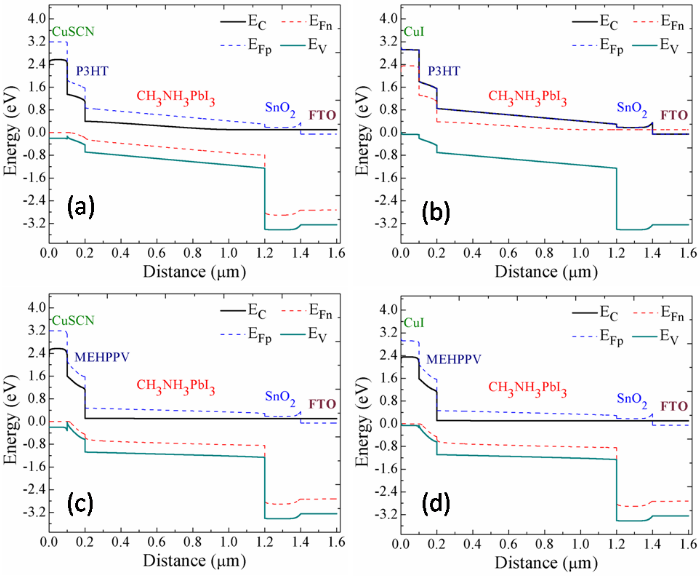

Figure 3: Energy band diagram of: a) $SnO_2/CH_3NH_3PbI_3/P_3HT/CuSCN/Au$, b) $SnO_2/CH_3NH_3PbI_3/P_3HT/CuI/Au$, c) $SnO_2/CH_3NH_3PbI_3/MEHPPV/CuSCN/Au$, and d) $SnO_2/CH_3NH_3PbI_3/MEHPPV/CuI/Au$, showing their conduction band (Ec), valence band (Ev), and Fermi levels (E_{fn}, E_{fp})

Energy bandgap diagram

The transition of photo-generated carriers from the valence band to the conduction band plays a crucial role in determining the performance of perovskite solar cells, particularly when paired with various carrier transport layers [37]. This relationship underscores the importance of optimizing carrier dynamics to enhance device efficiency and overall energy conversion effectiveness. In Figure 3, the energy band diagrams of the four proposed perovskite solar cells (PSCs) are illustrated showing their valance band, conduction band and Fermi levels. Here, fluorine-doped tin oxide (FTO) performs the function of a front contact window layer and a transparent conductive oxide for light passage [3,28,29]. The conduction band and valence band energies are represented as Ec and Ev, respectively. Moreover, E_{Fn} and E_{Fp} indicate the Fermi levels for n-type and p-type semiconductors, as shown in Figure 3 (a, b, c, and d). Figures 3a and 3b depict the energy band diagrams for the respective layers of $SnO_2/CH_3NH_3PbI_3/P_3HT/CuSCN/Au$ and $SnO_2/CH_3NH_3PbI_3/P_3HT/CuI/Au$ PSCs. Figures 3c and 3d shows the energy band diagrams for the respective layers of $SnO_2/CH_3NH_3PbI_3/MEHPPV/CuSCN/Au$ PSC and $SnO_2/CH_3NH_3PbI_3/MEHPPV/CuI/Au$ PSC. The incorporation of organic/inorganic hole transport layer effects is evident in the band diagrams of all four perovskite structures. It has been observed that both organic and inorganic HTL layers impact the band diagrams. For effective separation of photogenerated holes and electrons, the band edges of the transport layers must be appropriately designed. The power conversion efficiency of the devices is influenced by the band bending at the perovskite/HTL interface due to higher built-in potentials. To facilitate electron collection at the first junction, the conduction band of the electron transport layer must align with that of the absorber layer. Furthermore, the bandgap of the ETL layer must be greater than that of the absorber layer. This gives rise to a barrier that allows the absorber layer to gather electrons while blocking holes. The high bandgap of the ETL layer ensures it can capture numerous photons effectively at the absorption surface. Simultaneously, the valence band of the HTL (p+ layer) must match that of the absorber layer at the second junction, which aids in hole collection while preventing electron flow. As detailed in Table 1, the thickness of each layer is 1 µm for $CH_3NH_3PbI_3$, while the organic and HTL layers are 100 nm thick. The SnO_2 layer is also 100 nm thick. The energy range is swept from -3.2 eV to 4 eV, and the distance varies from 0 to 1.6 µm, as illustrated in Figure 3. The energy profile for the PSC that uses the P_3HT layer displays a similar overall shape, but the energy curve has altered due to the HTL layer, including shifts in Ec, Ev, EFn, and E_{Fp}. The addition of the CuI layer shifts E_{Fn} to a higher energy value and Ec to even higher energy levels, as represented in Figure 3a and 3b. Notably, Ec-E_{Fn} is extended in the $SnO_2/CH_3NH_3PbI_3/P_3HT/CuI/Au$ PSC, while Ev-E_{Fp} remains unchanged. The inclusion of CuI lowers E_{Fp} for the PSC based on MEHPPV, causing the Ev profile to shift within the 0-0.2 µm range, contributing to a gradual incline in the Ev curve as shown in Figure 3c and 3d. It has been reported that the direct optical bandgap energy ranges between 3.60 and 4.20 eV, while the indirect optical bandgap energy lies between 2.36 eV and 3.20 eV when CuSCN is doped with lithium [38]. However, the bandgap of $CH_3NH_3PbI_3$ is approximately 1.5 eV. The high PCE of $CH_3NH_3PbI_3$ in solar cells can be attributed to its excellent ambipolar charge transport, long electron-hole diffusion lengths, good radiative efficiency, photon recycling capabilities, high optical absorption coefficient, and low exciton binding energy. Therefore, the ETL layer's bandgap must be greater than that of the absorber layer, with $CH_3NH_3PbI_3$ serving as the absorber in this context [39]. The energy disparity between the valence band of the perovskite and the HTL establishes an energy barrier that enhances the transport of holes from the perovskite to the hole transport material (HTM). As illustrated in the band diagrams presented in Figure 3, the valence band of the perovskite is located at a lower energy level than that of the HTL. A more pronounced energy barrier can be achieved by utilizing the proposed band-gap of the organic/inorganic HTL. Solar cell architectures that incorporate these HTLs demonstrate the highest power conversion efficiency due to their minimized activation energy related to interfacial recombination. To facilitate efficient hole extraction, the highest occupied molecular orbital (HOMO) level of the HTL must exceed that of the valence band of the perovskite layer [37]. According to reports by Cassas *et al.*, the bandgap of $CH_3NH_3PbI_3$ is 1.55 eV, while Mandadapu *et al.* noted it as 1.730 eV [40,41]. CuI is characterized as a p-type transparent conductive semiconductor that possesses distinctive optoelectronic features, including a wide bandgap of 3.1 eV, strong hole mobility (greater than 40 $cm^2/V{\cdot}s$ in bulk), and a significant exciton binding energy of 62 meV at room temperature [42]. Furthermore, MEHPPV, or poly[2-methoxy-5-1,4-phenylene-vinylene], is a p-type semiconducting material with a bandgap of 2.2 eV, which is being explored for the formation of p-n junctions, particularly with n-type materials like PCBM, to create high-efficiency photovoltaic cells from polymers. P_3HT is another p-type polymer semiconductor with a bandgap of 2 eV, belonging to the polythiophene family, and it is actively researched for use in diodes development [43,44].

Band gap variation of HTL

Figure 4 demonstrates how the band gap of CuSCN, functioning as a hole transport layer (HTL), affects the photovoltaic parameters of the proposed solar cells. The band gap of CuSCN is varied between 3.0 and 3.8 eV. Figure 4a illustrates that the open-circuit voltage (Voc) remains constant at 1.159 V, while the short-circuit current density (Jsc) increases slightly from 25.356 to 25.359 mA/cm^2 with an increase in the CuSCN band gap up to 3.6 eV for the $SnO_2/CH_3NH_3PbI_3/P_3HT/CuSCN/Au$ perovskite solar cells (PSCs). The fill factor (FF) increases from 54.35% to 77.20%, and the power conversion efficiency (PCE) rises from 15.97% to 22.69% until the band gap reaches 3.6 eV, after which both values begin to decline, as shown in Figure 4b.

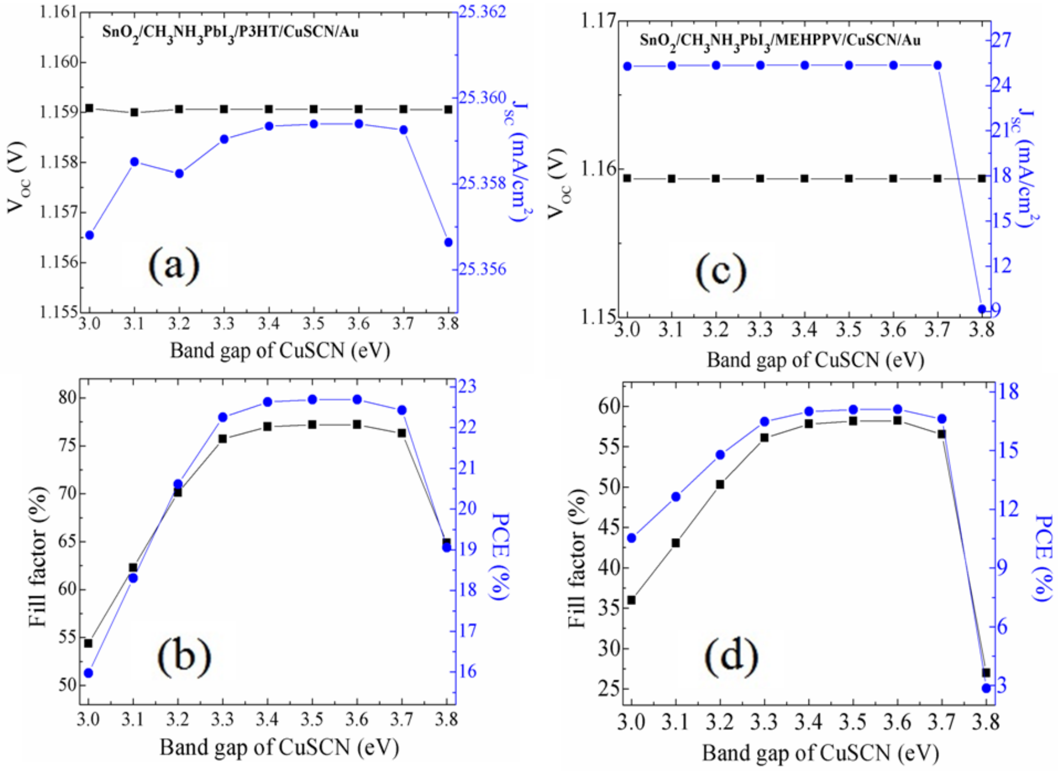

Figure 4: Photovoltaic parameters as a function of the bandgap of CuSCN, a) Voc and Jsc, b) FF and PCE for $SnO_2/CH_3NH_3PbI_3/P_3HT/CuSCN/Au$, c) Voc and Jsc, and d) FF and PCE for $SnO_2/CH_3NH_3PbI_3/MEHPPV/CuSCN/Au$

The increase in Jsc is attributed to enhanced electron-hole pair generation due to the elevated band gap of the HTL. Similarly, Figure 4c shows that Voc remains constant at 1.159 V as the band gap of CuSCN increases. However, Jsc rises from 25.27 to 25.35 mA/cm^2 between 3.0 - 3.6 eV and decreases at 3.7 eV for the $SnO_2/CH_3NH_3PbI_3/MEHPPV/CuSCN/Au$ PSC. Figure 4d indicates that both the values of FF (35.96% to 58.21%) and PCE (10.53% to 17.10%) for this PSC increase until the CuSCN band gap reaches 3.6 eV, after which they also decline. In conclusion, the optimal band gap of CuSCN for achieving maximum efficiency in both PSCs is 3.6 eV. The effect of the band-gap of CuI as an HTL on the photovoltaic parameters of the proposed PSCs is illustrated in Figure 5. The band-gap of CuI varies between 2.7 eV and 3.3 eV.

In Figure 5a, it can be observed that the Voc remains consistent at 1.159 V as the band-gap of CuI increases for the $SnO_2/CH_3NH_3PbI_3/P_3HT/CuI/Au$ PSC. The Jsc experiences a marginal increase from 25.356-25.359 mA/cm^2 between the bandgap of 2.7 eV to 3.1 eV, but decreases from 3.2 eV. The FF ranges from 57.21% to 76.39%, and the PCE increases from 16.81% to 22.45% until the band-gap reaches 3.1 eV, after which both parameters decline, as shown in Figure 5b.

The improvement in Jsc is attributed to the enhanced generation of electron-hole pairs resulting from the increased band-gap of the HTL.

Similarly, Figure 5c indicates that Voc remains unchanged as the CuI band-gap increases; however, Jsc rises from 25.288 mA/cm^2 to 25.347 mA/cm^2 between 2.7 eV and 3.1 eV bandgap. The Jsc starts decreasing at 3.2 eV for the $SnO_2/CH_3NH_3PbI_3/MEHPPV/CuSCN/Au$ PSC. Figure 5d shows that both FF (ranging from 38.43% to 57.15%) and PCE (from 11.26% to 16.79%) for the $SnO_2/CH_3NH_3PbI_3/MEHPPV/CuI/Au$ PSC improve until the band-gap reaches 3.1 eV, after which they decline.

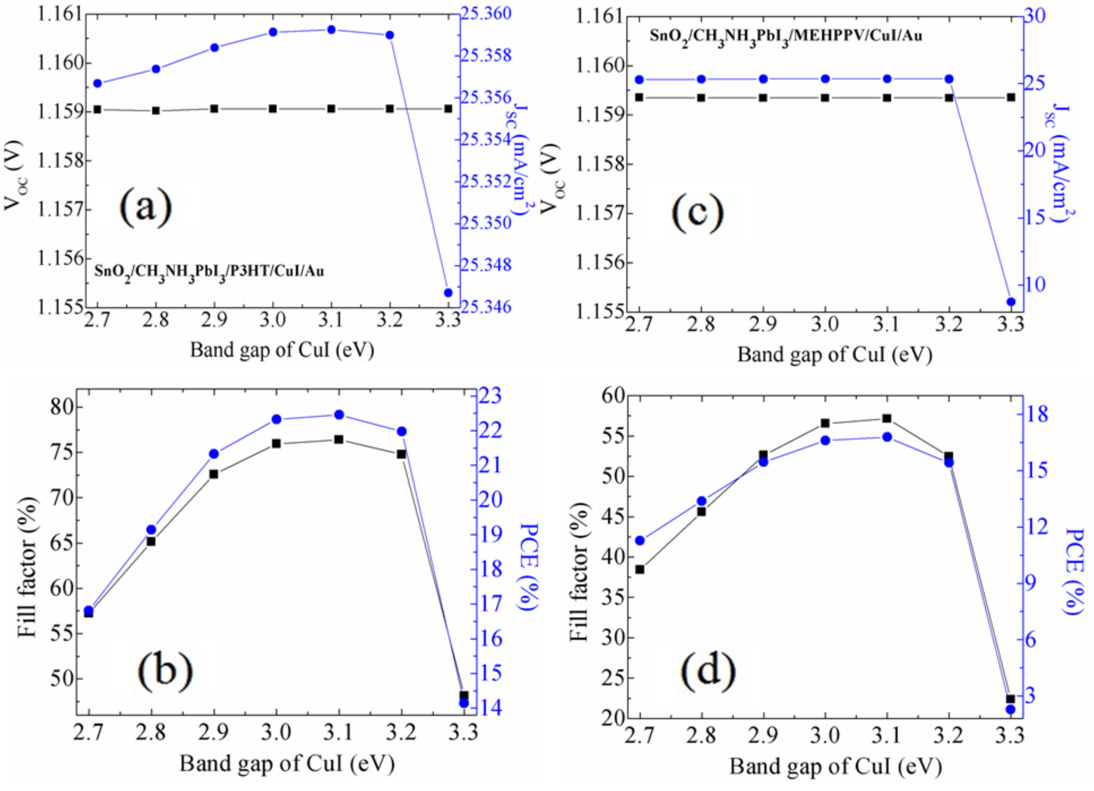

Figure 5: Photovoltaic parameters as a function of the bandgap of CuI, a) Voc and Jsc, b) FF and PCE for $SnO_2/CH_3NH_3PbI_3/P_3HT/CuI/Au$, c) Voc and Jsc, and d) FF and PCE for $SnO_2/CH_3NH_3PbI_3/MEHPPV/CuI/Au$ PSC

The enhancement in FF and PCE for both PSCs is a result of the increased Jsc. The optimum bandgap of CuI is 3.1 eV. This increase is due to the high work functions of CuSCN and CuI, which create an ohmic contact at the perovskite/HTL interface. This relationship underscores a favorable condition for the reduction of charge recombination, which is largely due to the precise energy-level alignment achieved between the organic and inorganic layers and the perovskite structure. Such alignment fosters an effective interaction that maximizes energy utilization, ultimately enhancing overall device performance. The optimum band-gap of CuI for achieving maximum efficiency in both PSCs is 3.2 eV. However, there is a risk of charge recombination due to the proper energy-level alignment between CuSCN/CuI and the perovskite structure. The energy band-gap of the HTL determines its corresponding highest occupied molecular orbital (HOMO) level; a higher HOMO level in the HTL facilitates the efficient extraction of positive charge carriers from the perovskite [45-46].

The variation in band-gap is contingent upon the thin film deposition technique and the specific conditions employed during the process. This band-gap alteration is significantly associated with the dependence of electronic states on factors such as the effective exciton mass, dielectric confinement, and quantum confinement in ultrathin films. Moreover, the alignment of energy bands at the interface between the HTL and the perovskite layer, combined with the formation of vacancies within the HTL, plays a crucial role in mitigating dangling bonds and trapping states [47].

In numerous prior simulation studies, the band gap of copper thiocyanate (CuSCN) has been observed to range between 3.4 and 3.9 eV, particularly in the context of thin films [48,49].

In comparison, the band gap of copper iodide (CuI) thin films, characterized by nanometer thickness, has been documented to lie between 2.9 and 3.5 eV, as indicated by both theoretical and experimental research findings [50,51].

The variation in band gap is influenced significantly by the deposition techniques and the specific conditions employed during the thin film fabrication process. This band gap alteration is fundamentally associated with the strong dependence of electronic states on several factors, including effective exciton mass, dielectric confinement, and quantum confinement present in ultrathin films [37].

Band gap variation of organic layer

The effect of P_3HT's band-gap on the photovoltaic parameters of the proposed perovskite solar cells (PSCs) is illustrated in Figure 6.

The band-gap of P_3HT ranges from 1.7 eV to 2.3 eV. As shown in Figure 6a, the open-circuit voltage (Voc) decreases from 1.159 V to 1.155 V as the band-gap of P_3HT increases for the $SnO_2/CH_3NH_3PbI_3/P_3HT/CuSCN/Au$ PSC. In addition, the short-circuit current density (Jsc) experiences a slight decrease from 25.37 mA/cm^2 to 25.35 mA/cm^2 with an increasing band-gap of P_3HT.

Figure 6b indicates that both the FF and PCE initially increase until the band-gap reaches 2.0 eV, after which both parameters begin to decline. At a band-gap of 2.0 eV, the FF value is 76.99%, and the PCE value is 22.63%.

In Figure 6c, a comparable trend is observed for the $SnO_2/CH_3NH_3PbI_3/P_3HT/CuI/Au$ PSC. The Voc value decreases from 1.159 V to 1.155 V as the band gap of P_3HT increases. The Jsc value shows a slight reduction, dropping from 25.37 mA/cm^2 to 25.35 mA/cm^2 with the increase in band gap. Furthermore, the FF and PCE values improve until the band gap reaches 2.0 eV, after which they begin to decline, as illustrated in Figure 6d.

The optimum band gap of P_3HT is 2.0 eV, where the FF is 75.64%, and the PCE is 22.23%. The influence of the band gap of MEHPPV on the photovoltaic parameters of the proposed perovskite solar cells is presented in Figure 7.

The band gap of MEHPPV varies between 2.1 eV and 2.6 eV. As illustrated in Figure 7a, the Voc demonstrates a reduction from 1.159 V to 1.155 V as the band gap of MEHPPV increases within the $SnO_2/CH_3NH_3PbI_3/MEHPPV/CuSCN/Au$ PSC configuration. Concurrently, the Jsc exhibits a slight increase from 25.32 mA/cm^2 to 25.35 mA/cm^2 in response to the rising band gap of MEHPPV.

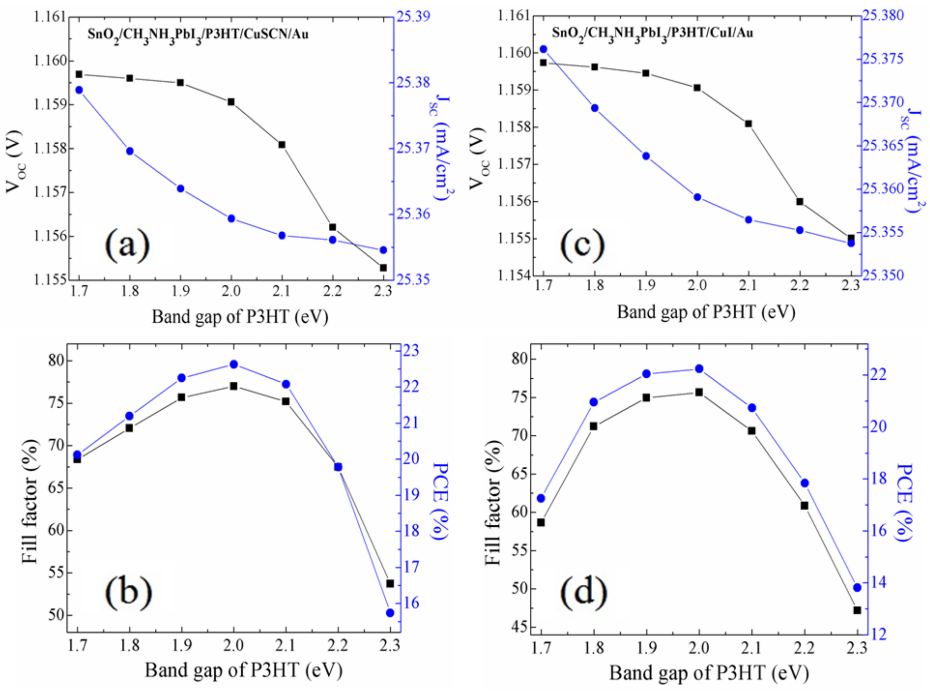

Figure 6: Photovoltaic parameters as a function of the bandgap of P$_3$HT, a) Voc and Jsc, b) FF and PCE for SnO$_2$/CH$_3$NH$_3$PbI$_3$/P$_3$HT/CuSCN/Au, c) Voc and Jsc, and d) FF and PCE for SnO$_2$/CH$_3$NH$_3$PbI$_3$/P$_3$HT/CuI/Au

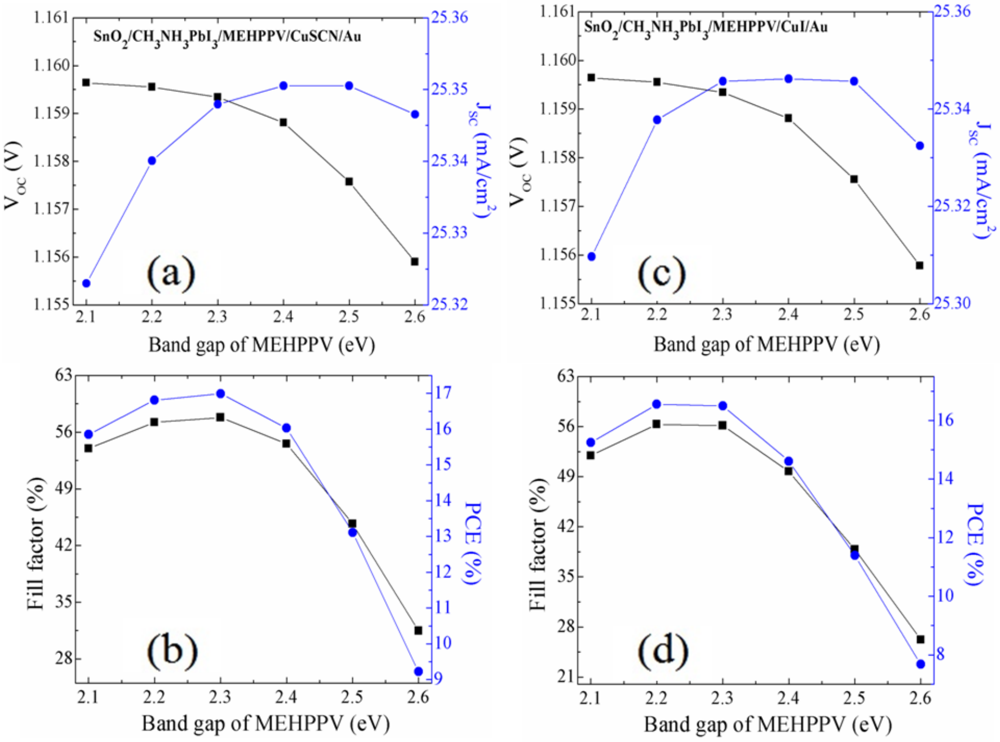

Figure 7: Photovoltaic parameters as a function of bandgap of MEHPPV, a) Voc and Jsc, b) FF and PCE for SnO$_2$/CH$_3$NH$_3$PbI$_3$/MEHPPV/CuSCN/Au; c) Voc and Jsc, d) FF and PCE for SnO$_2$/CH$_3$NH$_3$PbI$_3$/MEHPPV/CuI/Au

The FF and PCE show an initial increase until the band gap reaches 2.3 eV, at which point both parameters begin to decline, as demonstrated in Figure 7b. At a band gap of 2.3 eV, the FF is recorded at 57.81%, while the PCE is 16.98%.

Figure 7c reveals a similar pattern for the $SnO_2/CH_3NH_3PbI_3$/MEHPPV/CuI/Au PSC, where the Voc decreases from 1.159 V to 1.155 V with an increasing MEHPPV band gap. The Jsc experiences a marginal increase from 25.30 mA/cm^2 to 25.34 mA/cm^2 as the band gap is elevated from 2.1 eV to 2.4 eV. However, further escalation of the MEHPPV band gap leads to a subsequent decrease in Jsc. Consistent with previous observations, both the FF and PCE increase until the band gap reaches 2.3 eV, after which they decline, as indicated in Figure 7d.

The optimum band gap of MEHPPV is 2.3 eV, where the FF is reported at 56.13%, and the PCE is noted at 16.49%. The bandgap of the organic layer plays a critical role in influencing the efficiency of photon energy transfer to the junction, thereby enhancing the photon flux. The incident photon-to-current conversion efficiency (IPCE) of the FTO/bl-TiO_2/m-$TiO_2/CH_3NH_3PbI_3$/CuSCN/Au device demonstrated comparable power conversion efficiency within the wavelength range of 400-500 nm, aligning with the findings of our study [8].

Furthermore, Thakur *et al.* [52] investigated the effects of the bandgap of the interface layers on the performance characteristics of $CH_3NH_3PbI_3$-based perovskite solar cells.

Effect of organic layer thickness

Figure 8 shows that the photovoltaic parameters of the PSCs are studied as a function of organic layers thickness. The thickness of the organic layer P_3HT varies between 10 nm and 100 nm. As depicted in Figure 8a, in the $SnO_2/CH_3NH_3PbI_3/P_3HT$/CuSCN/Au PSC, the Voc remains constant at 1.159 V, while the Jsc shows a marginal increase from 25.355-25.359 mA/cm^2 when the thickness of P_3HT varies. Consequently, both the FF and the PCE decrease with changes in P_3HT thickness, as illustrated in Figure 8b.

The optimal P_3HT thickness is found to be 10 nm, achieving the highest FF of 82.66% and PCE of 24.29%. In the $SnO_2/CH_3NH_3PbI_3/P_3HT$/CuI/Au PSC, as depicted in Figure 8c, Voc remains constant at 1.159 V, while the Jsc shows a marginal increase from 25.355-25.359 mA/cm^2 when the thickness of P_3HT varies. However, similar to the previous case, the FF and PCE decrease with increasing thickness, as shown in Figure 8d.

Likewise, the optimum P_3HT thickness is 10 nm, resulting in a FF value of 81.81% and PCE of 24.04%. This fact highlights the use of a more efficient PSC that is based on layers of P_3HT and CuSCN. The thickness of the organic layer MEHPPV varies between 10 nm and 100 nm, significantly influencing the performance of PSCs.

In Figure 9a, we observe that within the $SnO_2/CH_3NH_3PbI_3$/MEHPPV/CuSCN/Au configuration, the Voc experiences a negligible increase (1.15951-1.15955 V) as the MEHPPV thickness is varied, while the Jsc decreases from 25.356-25.34 mA/cm^2. This behavior leads to a noteworthy decline in both the FF (77.86-57.21%) and the PCE (22.89-16.81%), as illustrated in Figure 9b.

Remarkably, the optimal MEHPPV thickness is found to be as low as 10 nm, achieving a peak efficiency of 22.89%, which highlights the importance of precise layer control. In contrast, when examining the $SnO_2/CH_3NH_3PbI_3$/MEHPPV/CuI/Au PSC, depicted in Figure 9c, the Voc experiences a negligible increase (1.15952-1.15955 V) as the MEHPPV thickness is varied, while the Jsc decreases from 25.35-25.33 mA/cm^2. Akin to the previous case with increasing thickness, both the FF (77.18-56.33%) and the PCE (22.69-16.55%) declines as demonstrated in Figure 9d, suggesting a more favorable response to thickness changes in this configuration. Once again, the optimal thickness is noted at 10 nm, achieving an impressive efficiency of 22.69%. This compelling data underscores the critical role of P_3HT and MEHPPV thickness on the overall performance of PSCs, revealing the delicate balance between material properties and solar cell efficiency.

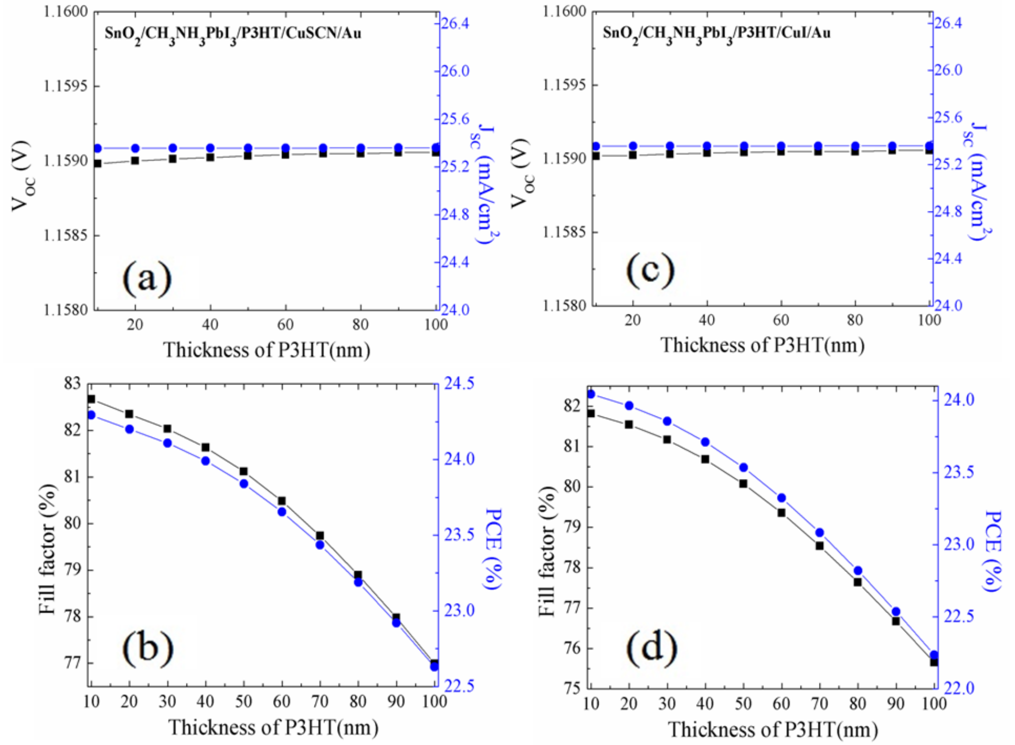

Figure 8: Photovoltaic parameters as a function of P$_3$HT thickness, a) Voc and Jsc, b) FF and PCE for SnO$_2$/CH$_3$NH$_3$PbI$_3$/P$_3$HT/CuSCN/Au, c) Voc and Jsc, and d) FF and PCE for SnO$_2$/CH$_3$NH$_3$PbI$_3$/P$_3$HT/CuI/Au

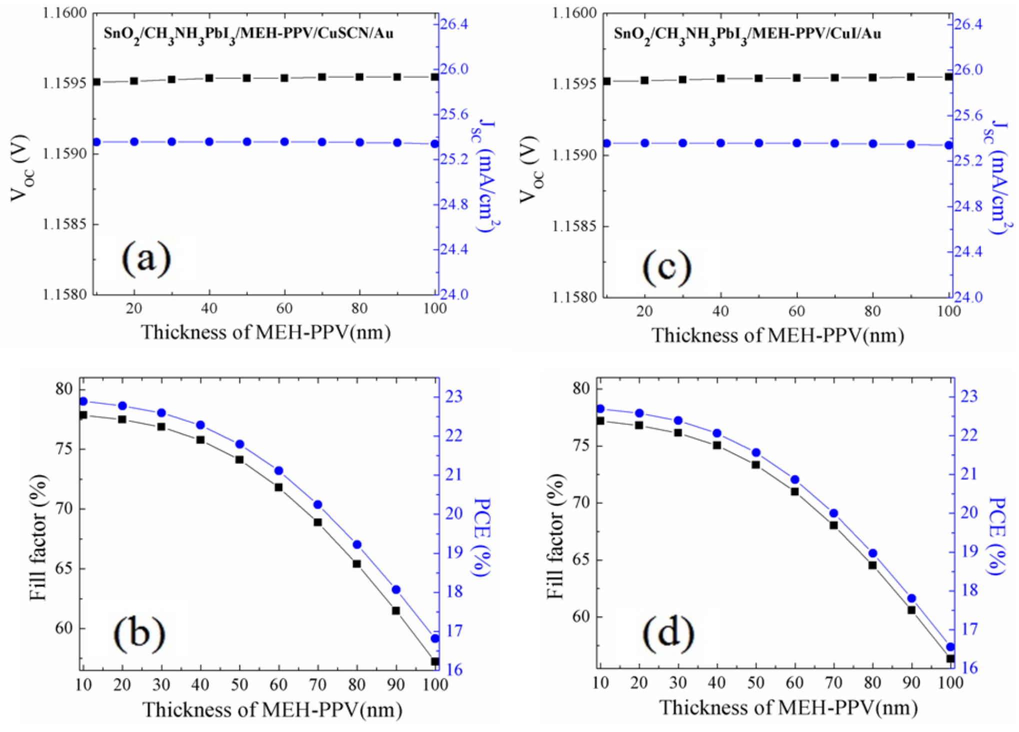

Figure 9: Photovoltaic parameters as a function of MEHPPV thickness, a) Voc and Jsc, b) FF and PCE for SnO$_2$/CH$_3$NH$_3$PbI$_3$/MEHPPV/CuSCN/Au, c) Voc and Jsc, and d) FF and PCE for SnO$_2$/CH$_3$NH$_3$PbI$_3$/MEHPPV/CuI/Au

The thickness optimization of the organic layer significantly enhances photon absorption, leading to improved carrier generation. This modification not only boosts the probability of generating more electron-hole pairs, but also effectively minimizes the recombination process [53]. The reduced thickness of the hole transport layer (HTL) often leads to diminished series resistance, thereby enhancing the overall performance of the solar cell [47].

Consequently, a default thickness of 10 nm is proposed for the organic layer to optimize power conversion efficiency. P_3HT and MEHPPV are considered as effective materials for charge transport and electron acceptance, as they contribute to a reduction in undesirable charge carrier recombination as well as leakage currents. The maintenance of a low thickness in the organic layer is advantageous due to its high transparency and improved photovoltaic performance [47,54]. Recent findings assert that perovskite solar cells with active areas larger than 10 cm^2 exhibit remarkable performance metrics. In particular, the FTO/c-TiO_2/m-TiO_2/$MAPbI_3$/Spiro-OMeTAD/Au configuration has achieved an exceptional open-circuit voltage of 38.6 V and a short-circuit current density of 18.12 mA/cm^2 [55]. On the other hand, the PDMS/PEDOT:PSS/PVK/$PC_{61}BM$/PEI/PEDOT:PSS/PDMS structure recorded the lowest Voc at 2.12 V, with a Jsc of 5.89 mA/cm^2, leading to an efficiency of 7.91% [56].

Moreover, previous studies have clearly demonstrated that the heterostructures FTO/TiO_2/$CH_3NH_3PbI_{3-x}Cl_x$/spiro-OMeTAD and FTO/TiO_2/$CH_3NH_3PbI_xCl_x$/CuSCN achieved a Voc of 1.5 V and a fill factor (FF) of 90%, which can be directly, linked to the thickness of the CuSCN layers, with a PCE reaching just below 32% [57-60]. These results are consistent with our findings, further solidifying the performance capabilities of PSCs.

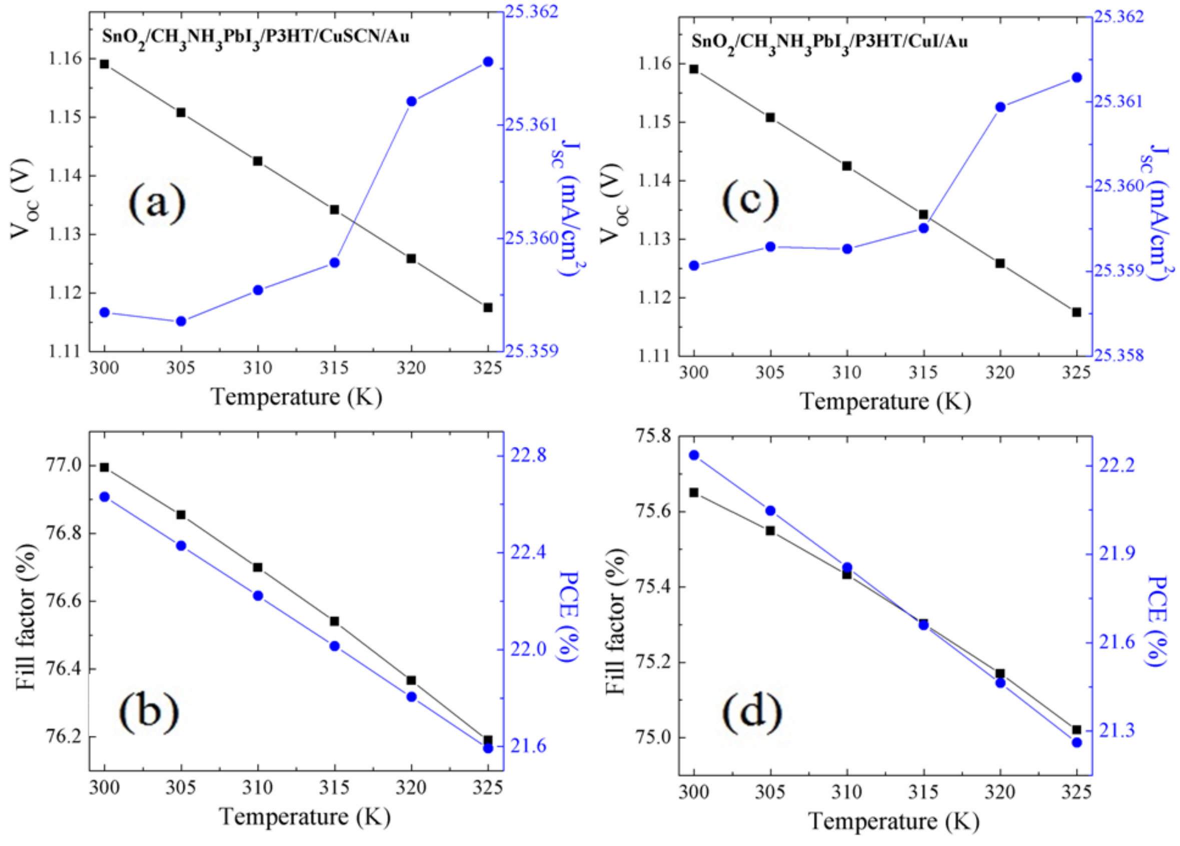

Figure 10: Photovoltaic parameters as a function of temperature, a) Voc and Jsc, b) FF and PCE for SnO_2/$CH_3NH_3PbI_3$/P_3HT/CuSCN/Au, c) Voc and Jsc, and d) FF and PCE for SnO_2/$CH_3NH_3PbI_3$/P_3HT/CuI/Au

Effect of temperature

The effects of temperature variation on the proposed $CH_3NH_3PbI_3$ perovskite solar cells are analyzed by changing the hole transport layer in different organic layer combinations. The temperature profiles for the configurations $SnO_2/CH_3NH_3PbI_3$/P3HT/CuSCN/Au and $SnO_2/CH_3NH_3PbI_3$/P3HT/CuI/Au are presented in Figure 10. The temperature was varied between 300-325 K. Figure 10a illustrates the decrease in Voc from 1.16 V to 1.11 V as the temperature increases but Jsc increases from 25.35-25.36 mA/cm^2 in $SnO_2/CH_3NH_3PbI_3$/P3HT/CuSCN/Au perovskite solar cell. The FF (76.99-76.18%) declines along with PCE (22.63-21.59%), as demonstrated in Figure 10b. The simulated structure achieves an optimized efficiency at 300 K. Similarly, Figure 10c depicts a decrease in Voc from 1.159 V to 1.117 V with rising temperatures, while Jsc shows a marginal increase from 25.359-25.361 mA/cm^2 in the $SnO_2/CH_3NH_3PbI_3/P_3HT$/CuI/Au PSC. Again, both FF and PCE decrease with increasing temperature, as illustrated in Figure 10d. This simulated structure has a PCE of 22.23% and a fill factor of 75.64% at 300K. Overall, the combination of perovskite with P_3HT and CuSCN may offer a promising approach to enhance the photovoltaic properties of PSC devices at room temperature for enhanced efficiency. The performance of photovoltaic solar cells is considerably influenced by environmental factors, particularly temperature. This study indicates that the proposed solar cell design exhibits optimized efficiency in regions characterized by low temperatures. Likewise, the temperature profiles for the configurations $SnO_2/CH_3NH_3PbI_3$/MEHPPV/CuSCN/Au and $SnO_2/CH_3NH_3PbI_3$/MEHPPV/CuI/Au are shown in Figure 11.

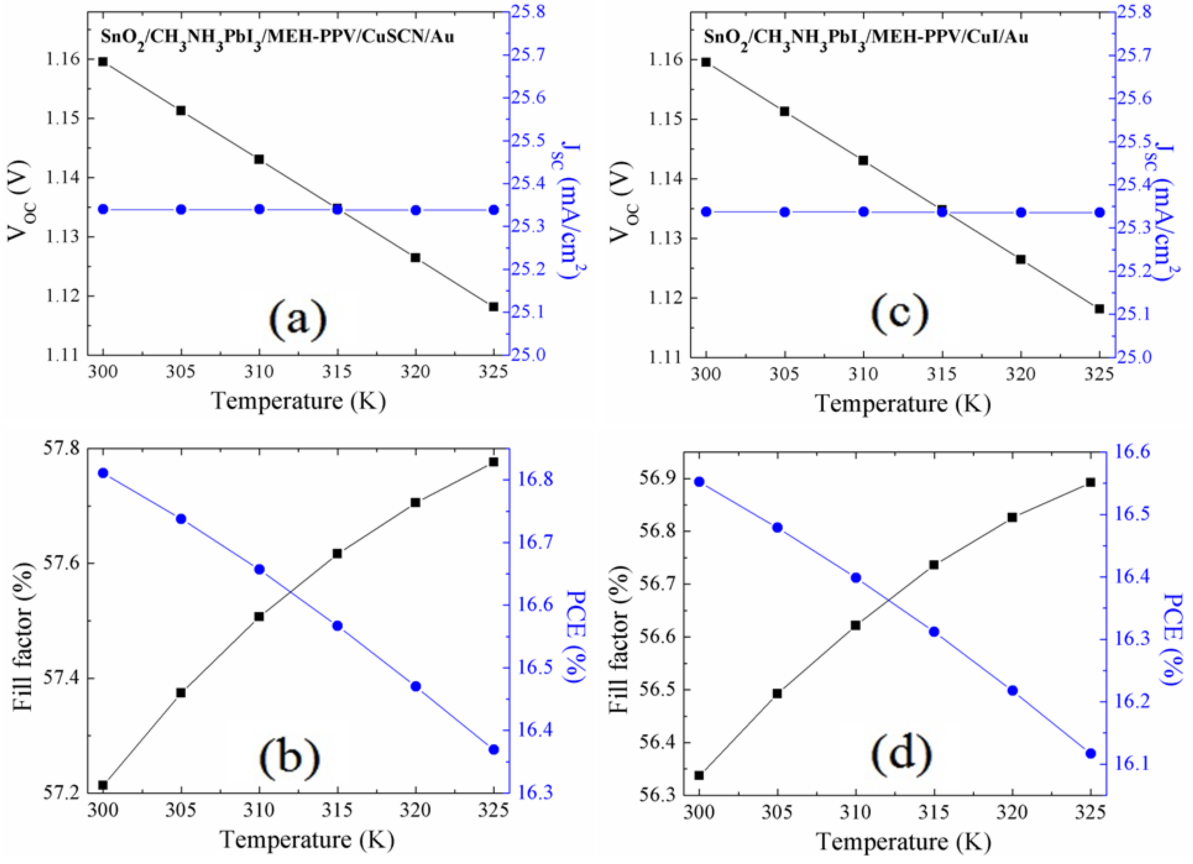

Figure 11: Photovoltaic parameters as a function of temperature, a) Voc and Jsc, b) FF and PCE for $SnO_2/CH_3NH_3PbI_3$/MEHPPV/CuSCN/Au; c) Voc and Jsc, and d) FF and PCE for $SnO_2/CH_3NH_3PbI_3$/MEHPPV/CuI/Au

Figure 11a demonstrates that the Voc decreases from 1.16 V to 1.12 V as the temperature rises, while the Jsc decreases from 25.35-25.34 mA/cm² in the $SnO_2/CH_3NH_3PbI_3$/MEHPPV/CuSCN/Au PSC.

Figure 11b shows a marginal increase in the FF, from 57.21% to 57.77%, while the PCE declines from 16.81% to 16.36% with rising temperature. In addition, Figure 11c confirms that Voc remains constant at 1.159 V, but Jsc decreases from 25.35-25.33 mA/cm² in the $SnO_2/CH_3NH_3PbI_3$/MEHPPV/CuI/Au PSC. Figure 11d indicates a decrease in FF, from 77.18% to 56.33%, but PCE decreases from 22.69 to 16.55% as temperature increases. The current density decreases at higher temperatures because re-combination processes occur more rapidly, resulting in less values for photovoltaic voltage and fill factor. At lower temperatures, reverse bias reduce leakage currents and enhance device quality. In contrast, higher temperatures lead to increased leakage currents and a higher risk of thermal breakdown. Overall, lower temperatures improve performance and stability, while higher temperatures contribute to degradation [61,62]. It is clear that for both types of PSCs, the optimal operating temperature is room temperature (300K), exceeding this temperature leads to a significant reduction in PCE. This observation highlights the critical need for thermal management in the design of solar cells [52].

C-V characteristics

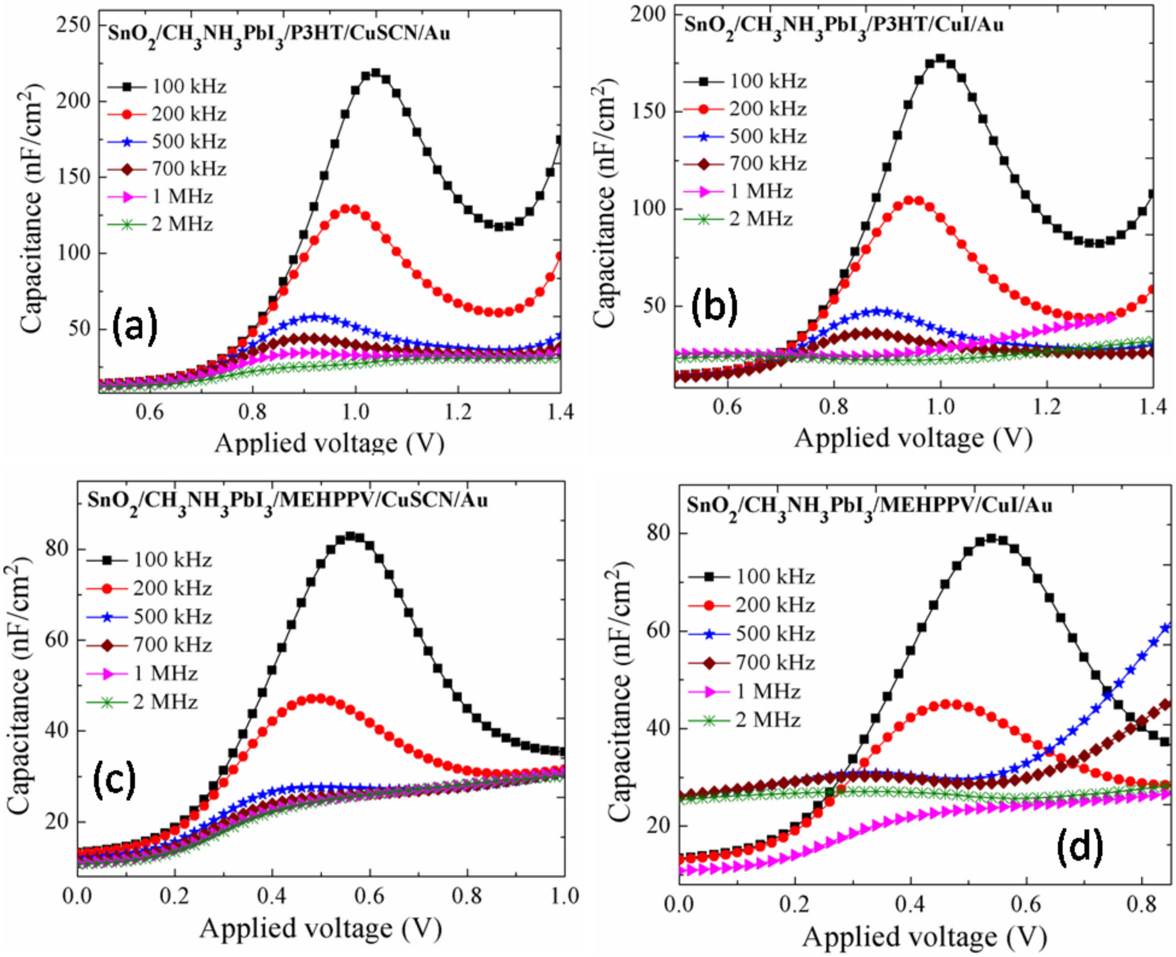

Figure 12: Capacitance-voltage plots of different PSCs at different frequencies, a) $SnO_2/CH_3NH_3PbI_3/P_3HT$/CuSCN/Au, b) $SnO_2/CH_3NH_3PbI_3/P_3HT$/CuI/Au, c) $SnO_2/CH_3NH_3PbI_3$/MEHPPV/CuSCN/Au, and d) $SnO_2/CH_3NH_3PbI_3$/MEHPPV/CuI/Au

The capacitance-voltage (C-V) characteristics of the proposed four PSCs are effectively plotted within a voltage range of 0.5 V to 1.4 V, encompassing a frequency range of 100 kHz to 2 MHz. The depletion and accumulation effects are distinctly observed within the forward bias range, clearly demonstrating the performance of these devices. In Figure 12a, the $SnO_2/CH_3NH_3PbI_3/P_3HT/CuSCN/Au$ perovskite solar cell exhibits a capacitance of 218 nF/cm^2 at 1.04 V when measured at a frequency of 100 kHz. As the voltage increases within the biasing range of 0.5 V to 1.4 V, the capacitance shifts to lower values, measuring 130 nF/cm^2 at 200 kHz and 60 nF/cm^2 at 500 kHz. At lower frequencies (100-200 kHz), a noticeable oscillation in capacitance is observed, fluctuating between 125 and 225 nF/cm^2. The C-V profile is similar for PSCs that utilize CuI as the hole transport layer (HTL). However, the capacitance value is lower, reaching only 150 nF/cm^2. The C-V characteristics of the $SnO_2/CH_3NH_3PbI_3/P_3HT/CuI/Au$ structure exhibit several peaks at different frequencies, except at 1 MHz and 2 MHz. Two major peaks in the C-V curve appear at 100 kHz and 200 kHz, attributed to the inclusion of the CuI layer in the PSC heterostructure, as depicted in Figure 12b. At a fixed frequency of 100 kHz, the capacitance for PSCs with P_3HT reaches 220 nF/cm^2, compared to 125 nF/cm^2 for those with CuI and CuSCN HTL layers. At low frequencies, charges follow the alternating current signal to trapping centers, leading to an increase in capacitance within the solar cell device. This phenomenon can be explained by considering the severity of the series resistance in the accumulation zone, along with the potential importance of the interface density parameter in the deep depletion and depletion zones [63-65]. A notable change in the C-V curve occurs when the organic layer P_3HT is replaced with MEHPPV, as shown in Figures 12c and 12d. For PSCs based on MEHPPV, the capacitance values are lower, measuring 85 nF/cm^2 and 80 nF/cm^2 for CuSCN and CuI as HTL layers, respectively. Hence, in the accumulation region, the combination of P_3HT with CuSCN layers proves to be more effective for charge collection in our PSC device. Therefore, the optimal structure is $SnO_2/CH_3NH_3PbI_3/P_3HT/CuI/Au$. At higher frequencies (1 MHz and 2 MHz), a Mott-Schottky analysis for both fabricated and simulated devices at 1 kHz is reported. The $1/C^2$-V curve obtained from experimental results is roughly similar to that obtained through simulations, as previously reported for a PSC configuration with 17.5% efficiency, composed of $FTO/c\text{-}TiO_2/m\text{-}TiO_2$/perovskite/spiro/Au [66]. This advanced simulation technique will significantly enhance the synthesis and development of next-generation $CH_3NH_3PbI_3$ perovskite thin film solar cells, paving the way for more efficient and effective solar energy solutions.

Conclusion

This work presents a compelling study on the numerical optimization of a $SnO_2/CH_3NH_3PbI_3$/organic layer/HTL/Au solar cell through SCAPS-1D simulation. The present study critically examines the effects of various combinations of organic and inorganic hole transport layers (HTL), specifically P_3HT versus MEHPPV paired with CuSCN versus CuI, on the photovoltaic performance of $CH_3NH_3PbI_3$ perovskite solar cells. The findings unequivocally show that P_3HT emerges as a superior choice over MEHPPV for the organic layer, while CuSCN significantly outperforms CuI as the inorganic layer, culminating in the highest PCE of 22.63% with the $P_3HT/CuSCN$ configuration, compared to 22.23% with P_3HT/CuI. Moreover, the energy band diagrams demonstrate that the choice of P_3HT or MEHPPV and CuSCN or CuI at the $CH_3NH_3PbI_3$ interface is pivotal in optimizing performance. The bandgap energies of CuSCN, CuI, P_3HT and MEHPPV are fine-tuned for maximum efficiency. The bandgap of CuSCN, CuI, P_3HT and MEHPPV are optimized at 3.6, 3.1, 2.0, and 2.3 eV. Our analysis also reveals that maintaining the organic layer thickness within an optimal value of 10 nm is crucial for achieving Voc of 1.159 V, Jsc of 25.36 mA/cm^2, FF of 82.66% and PCE of 24.29% for $SnO_2/CH_3NH_3PbI_3/P_3HT/CuSCN/Au$ PSC. Importantly, we also observe that the photovoltaic performance of all proposed solar cells is optimum at 300K and deteriorates at elevated operating temperatures, a consideration that underscores the importance of thermal management in solar cell design. The capacitance-voltage (C-V) plots further illustrate a distinct peak in the accumulation region, with its position being dependent on the frequency, highlighting the intricate relationship between design parameters and performance. Overall, the $SnO_2/CH_3NH_3PbI_3/P_3HT/CuSCN/Au$ structure stands out as a highly promising candidate for future solar cell fabrication, paving the way for advancements in photovoltaic technology. This research not only enhances our understanding of material combinations, but also offers a roadmap for developing high-efficiency solar cells that can meet the demands of modern energy applications.

Acknowledgments

The authors would like to thank Prof. M. Burgelman and his co-workers, Department of Electronics and Information Systems, University of Gent, Belgium for providing the support of SCAPS simulation software. It is supported by 2022 PRFU PROJECT under contract B00L02UN310220220001.

Conflict of Interest

The authors declare that they have no conflict of interest in this study.

Orcid

Avishek Roy: *0000-0001-7784-1455*

Mostefa Benhaliliba: *0000-0001-6507-3663*

Asma Rahimi: *0009-0007-0070-3717*

Reference

[1]. M.K. Hossain, G.I. Toki, A. Kuddus, M.H. Rubel, M. Hossain, H. Bencherif, M.F. Rahman, M.R. Islam, M. Mushtaq, An extensive study on multiple ETL and HTL layers to design and simulation of high-performance lead-free CsSnCl3-based perovskite solar cells, *Scientific Reports*, **2023**, *13*, 2521. [Crossref], [Google Scholar], [Publisher]

[2]. Y. Gan, X. Bi, Y. Liu, B. Qin, Q. Li, Q. Jiang, P. Mo, Numerical investigation energy conversion performance of tin-based perovskite solar cells using cell capacitance simulator, *Energies*, **2020**, *13*, 5907. [Crossref], [Google Scholar], [Publisher]

[3]. E. Karimi, S. Ghorashi, Investigation of the influence of different hole-transporting materials on the performance of perovskite solar cells, *Optik*, **2017**, *130*, 650-658. [Crossref], [Google Scholar], [Publisher]

[4]. S.N. Habisreutinger, N.K. Noel, H.J. Snaith, Hysteresis index: A figure without merit for quantifying hysteresis in perovskite solar cells, *ACS Energy Letters*, **2018**, *3*, 2472-2476. [Crossref], [Google Scholar], [Publisher]

[5]. A. Kojima, K. Teshima, Y. Shirai, T. Miyasaka, Organometal halide perovskites as visible-light sensitizers for photovoltaic cells, *Journal of the American Chemical Society*, **2009**, *131*, 6050-6051. [Crossref], [Google Scholar], [Publisher]

[6]. B. Náfrádi, G. Náfrádi, L. Forró, E. Horváth, Methylammonium lead iodide for efficient X-ray energy conversion, *The Journal of Physical Chemistry C*, **2015**, *119*, 25204-25208. [Crossref], [Google Scholar], [Publisher]

[7]. S. Yakunin, D.N. Dirin, Y. Shynkarenko, V. Morad, I. Cherniukh, O. Nazarenko, D. Kreil, T. Nauser, M.V. Kovalenko, Detection of gamma photons using solution-grown single crystals of hybrid lead halide perovskites, *Nature Photonics*, **2016**, *10*, 585-589. [Crossref], [Google Scholar], [Publisher]

[8]. M. Birowosuto, D. Cortecchia, W. Drozdowski, K. Brylew, W. Lachmanski, A. Bruno, C. Soci, X-ray scintillation in lead halide perovskite crystals, *Scientific Reports*, **2016**, *6*, 37254. [Crossref], [Google Scholar], [Publisher]

[9]. B. Náfrádi, P. Szirmai, M. Spina, H. Lee, O. Yazyev, A. Arakcheeva, D. Chernyshov, M. Gibert, L. Forró, E. Horváth, Optically switched magnetism in photovoltaic perovskite CH3NH3 (Mn: Pb) I3, *Nature Communications*, **2016**, *7*, 13406. [Crossref], [Google Scholar], [Publisher]

[10]. M.I. Saidaminov, A.L. Abdelhady, B. Murali, E. Alarousu, V.M. Burlakov, W. Peng, I. Dursun, L. Wang, Y. He, G. Maculan, High-quality bulk hybrid perovskite single crystals within minutes by inverse temperature crystallization, *Nature Communications*, **2015**, *6*, 7586. [Crossref], [Google Scholar], [Publisher]

[11]. N. Yaacobi-Gross, N.D. Treat, P. Pattanasattayavong, H. Faber, A.K. Perumal, N. Stingelin, D.D. Bradley, P.N. Stavrinou, M. Heeney, T.D. Anthopoulos, High-efficiency organic photovoltaic cells based on the solution-processable hole transporting interlayer copper thiocyanate (CuSCN) as a replacement for PEDOT: PSS, *Advanced Energy Materials*, **2015**, *5*, 1401529. [Crossref], [Google Scholar], [Publisher]

[12]. G. Murugadoss, R. Thangamuthu, S.M.S. Kumar, Fabrication of CH3NH3PbI3 perovskite-based solar cells: Developing various new solvents for CuSCN hole transport material, *Solar Energy Materials and Solar Cells*, **2017**, *164*, 56-62. [Crossref], [Google Scholar], [Publisher]

[13]. P. Pattanasattayavong, G.O.N. Ndjawa, K. Zhao, K.W. Chou, N. Yaacobi-Gross, B.C. O'Regan, A. Amassian, T.D. Anthopoulos, Electric field-induced hole transport in copper (I) thiocyanate (CuSCN) thin-films processed from solution at room temperature, *Chemical Communications*, **2013**, *49*, 4154-4156. [Crossref], [Google Scholar], [Publisher]

[14]. P. Pattanasattayavong, N. Yaacobi-Gross, K. Zhao, G.O.N. Ndjawa, J. Li, F. Yan, B.C. O'Regan, A. Amassian, T.D. Anthopoulos, Hole-transporting transistors and circuits based on the transparent inorganic semiconductor copper (I) thiocyanate (CuSCN) processed from solution at room temperature, *Advanced Materials*, **2013**, *25*, 1504-1509. [Crossref], [Google Scholar], [Publisher]

[15]. K. Nithya, K. Sudheer, Device modelling of non-fullerene organic solar cell with inorganic CuI hole transport layer using SCAPS 1-D, *Optik*, **2020**, *217*, 164790. [Crossref], [Google Scholar], [Publisher]

[16]. K. Ramachandran, C. Jeganathan, G.P. Kalaignan, S. Karuppuchamy, Nanostructured bilayer CuSCN@ CuI thin films as efficient inorganic hole transport material for inverted perovskite solar cells, *Ceramics International*, **2021**, *47*, 17883-17894. [Crossref], [Google Scholar], [Publisher]

[17]. B. Zhang, Z. Genene, J. Wang, D. Wang, C. Zhao, J. Pan, D. Liu, W. Sun, J. Zhu, E. Wang, Facile Synthesis of Organic–Inorganic Hybrid Heterojunctions of Glycolated Conjugated Polymer-TiO$_{2}$− X for Efficient Photocatalytic Hydrogen Evolution, *Small*, **2024**, *20*, 2402649. [Crossref], [Google Scholar], [Publisher]

[18]. M. Ltayef, M.M. Almoneef, W. Taouali, M. Mbarek, K. Alimi, Conception and theoretical study of a new copolymer based on MEH-PPV and P3HT: enhancement of the optoelectronic properties for organic photovoltaic cells, *Polymers*, **2022**, *14*, 513. [Crossref], [Google Scholar], [Publisher]

[19]. S. Kumar, J. Kumar, S.N. Sharma, S. Srivastava, rGO integrated MEHPPV and P3HT polymer blends for bulk hetero junction solar cells: a comparative insight, *Optik*, **2019**, *178*, 411-421. [Crossref], [Google Scholar], [Publisher]

[20]. N. Singh, A. Agarwal, M. Agarwal, Numerical analysis of lead-free methyl ammonium tin halide perovskite solar cell, *AIP Conference Proceedings, AIP Publishing*, **2020**. [Crossref], [Google Scholar], [Publisher]

[21]. J. Kim, K.S. Kim, C.W. Myung, Efficient electron extraction of SnO2 electron transport layer for lead halide perovskite solar cell, *npj Computational Materials*, **2020**, *6*, 100. [Crossref], [Google Scholar], [Publisher]

[22]. S. Ghosh, S. Porwal, T. Singh, Investigation of the role of back contact work function for hole transporting layer free perovskite solar cells applications, *Optik*, **2022**, *256*, 168749. [Crossref], [Google Scholar], [Publisher]

[23]. M. Burgelman, K. Decock, S. Khelifi, A. Abass, Advanced electrical simulation of thin film solar cells, *Thin solid films*, **2013**, *535*, 296-301. [Crossref], [Google Scholar], [Publisher]

[24]. K. Decock, P. Zabierowski, M. Burgelman, Modeling metastabilities in chalcopyrite-based thin film solar cells, *Journal of Applied Physics*, **2012**, *111*. [Crossref], [Google Scholar], [Publisher]

[25]. J. Verschraegen, M. Burgelman, Numerical modeling of intra-band tunneling for heterojunction solar cells in SCAPS, *Thin Solid Films*, **2007**, *515*, 6276-6279. [Crossref], [Google Scholar], [Publisher]

[26]. J.A. Owolabi, M.Y. Onimisi, J.A. Ukwenya, A.B. Bature, U.R. Ushiekpan, Investigating the effect of ZnSe (ETM) and Cu2O (HTM) on absorber layer on the performance of pervoskite solar cell using SCAPS-1D, *Am. J. Phys. Appl.*, **2020**, *8*, 8-18. [Crossref], [Google Scholar], [Publisher]

[27]. F. Hazeghi, S.M.B. Ghorashi, Simulation of perovskite solar cells by using CuSCN as an inorganic hole-transport material, *Materials Research Express*, **2019**, *6*, 095527. [Crossref], [Google Scholar], [Publisher]

[28]. A. Raj, A. Anshul, V. Tuli, P.K. Singh, R.C. Singh, M. Kumar, Effect of appropriate ETL on quantum efficiency of double perovskite La2NiMnO6 based solar cell device via SCAPS simulation, *Materials Today: Proceedings*, **2021**, *47*, 1656-1659. [Crossref], [Google Scholar], [Publisher]

[29]. M. Ameri, M. Ghaffarkani, R.T. Ghahrizjani, N. Safari, E. Mohajerani, Phenomenological morphology design of hybrid organic-inorganic perovskite solar cell for high efficiency and less hysteresis, *Solar Energy Materials and Solar Cells*, **2020**, *205*, 110251. [Crossref], [Google Scholar], [Publisher]

[30]. E. Karimi, S.M.B. Ghorashi, The effect of SnO 2 and ZnO on the performance of perovskite solar cells, *Journal of Electronic Materials*, **2020**, *49*, 364-376. [Crossref], [Google Scholar], [Publisher]

[31]. S. Ahmed, F. Jannat, M.A.K. Khan, M.A. Alim, Numerical development of eco-friendly Cs2TiBr6 based perovskite solar cell with all-inorganic charge transport materials via SCAPS-1D, *Optik*, **2021**, *225*, 165765. [Crossref], [Google Scholar], [Publisher]

[32]. Y. Raoui, H. Ez-Zahraouy, N. Tahiri, O. El Bounagui, S. Ahmad, S. Kazim, Performance analysis of MAPbI3 based perovskite solar cells employing diverse charge selective contacts: Simulation study, *Solar Energy*, **2019**, *193*, 948-955. [Crossref], [Google Scholar], [Publisher]

[33]. K. Nithya, K. Sudheer, Device modelling of non-fullerene organic solar cell with inorganic CuI hole transport layer using SCAPS 1-D, *Optik*, **2020**, *217*, 164790. [Crossref], [Google Scholar], [Publisher]

[34]. A. Roy, A. Majumdar, Optoelectronic and surface properties of CuO clusters: thin film solar cell, *Journal of Materials Science: Materials in Electronics*, **2021**, *32*, 27823-27836. [Crossref], [Google Scholar], [Publisher]

[35]. C. Li, X. Chen, N. Li, J. Liu, B. Yuan, Y. Li, M. Wang, F. Xu, Y. Wu, B. Cao, Highly conductive n-type CH 3 NH 3 PbI 3 single crystals doped with bismuth donors, *Journal of Materials Chemistry C*, **2020**, *8*, 3694-3704. [Crossref], [Google Scholar], [Publisher]

[36]. I. Mohanty, S. Mangal, U.P. Singh, Influence of defect densities on perovskite (CH3NH3PbI3) solar Cells: Correlation of experiment and simulation, *Materials Today: Proceedings*, **2022**, *62*, 6199-6203. [Crossref], [Google Scholar], [Publisher]

[37]. A. Roy, A. Majumdar, Numerical optimization of Cu2O as HTM in lead-free perovskite solar cells: a study to improve device efficiency, *Journal of Electronic Materials*, **2023**, *52*, 2020-2033. [Crossref], [Google Scholar], [Publisher]

[38]. A. Abdulwahab, E.A. Al-Mahdi, A. Al-Osta, A. Qaid, Structural, optical and electrical properties of CuSCN nano-powders doped with Li for optoelectronic applications, *Chinese Journal of Physics*, **2021**, *73*, 479-492. [Crossref], [Google Scholar], [Publisher]

[39]. M.E. Ziffer, J.C. Mohammed, D.S. Ginger, Electroabsorption spectroscopy measurements of the exciton binding energy, electron–hole reduced effective mass, and band gap in the perovskite CH3NH3PbI3, *Acs Photonics*, **2016**, *3*, 1060-1068. [Crossref], [Google Scholar], [Publisher]

[40]. G. Casas, M.Á. Cappelletti, A.P. Cedola, B.M. Soucase, E.P. y Blancá, Analysis of the power conversion efficiency of perovskite solar cells with different materials as Hole-Transport Layer by numerical simulations, *Superlattices and Microstructures*, **2017**, *107*, 136-143. [Crossref], [Google Scholar], [Publisher]

[41]. U. Mandadapu, S.V. Vedanayakam, K. Thyagarajan, Simulation and analysis of lead based perovskite solar cell using SCAPS-1D, *Indian J. Sci. Technol*, **2017**, *10*, 1-8. [Crossref], [Google Scholar], [Publisher]

[42]. C. Yang, M. Kneiß, F.-L. Schein, M. Lorenz, M. Grundmann, Room-temperature domain-epitaxy of copper iodide thin films for transparent CuI/ZnO heterojunctions with high rectification ratios larger than 109, *Scientific reports*, **2016**, *6*, 21937. [Crossref], [Google Scholar], [Publisher]

[43]. S. Meftah, M. Benhaliliba, M. Kaleli, C. Benouis, C. Yavru, A. Bayram, Optical and electrical characterization of thin film MSP heterojunction based on organic material Al/p-Si/P3HT/Ag, *Physica B: Condensed Matter*,

2020, *593*, 412238. [Crossref], [Google Scholar], [Publisher]

[44]. S. Meftah, M. Benhaliliba, M. Kaleli, C. Benouis, C. Yavru, A. Bayram, Innovative organic MEH-PPV heterojunction device made by USP and PVD, *Journal of electronic materials*, **2021**, *50*, 2287-2294. [Crossref], [Google Scholar], [Publisher]

[45]. A. Kumar, S. Singh, Numerical modeling of planar lead free perovskite solar cell using tungsten disulfide (WS2) as an electron transport layer and Cu2O as a hole transport layer, *Modern Physics Letters B*, **2020**, *34*, 2050258. [Crossref], [Google Scholar], [Publisher]

[46]. B.A. Nejand, V. Ahmadi, S. Gharibzadeh, H.R. Shahverdi, Cuprous oxide as a potential low-cost hole-transport material for stable perovskite solar cells, *ChemSusChem*, **2016**, *9*, 302-313. [Crossref], [Google Scholar], [Publisher]

[47]. A. Roy, A. Majumdar, Optimization of CuO/CdTe/CdS/TiO2 solar cell efficiency: a numerical simulation modeling, *Optik*, **2022**, *251*, 168456. [Crossref], [Google Scholar], [Publisher]

[48]. J.-W. Liang, Y. Firdaus, C.H. Kang, J.-W. Min, J.-H. Min, R.H. Al Ibrahim, N. Wehbe, M.N. Hedhili, D. Kaltsas, L. Tsetseris, Chlorine-infused wide-band gap p-CuSCN/n-GaN heterojunction ultraviolet-light photodetectors, *ACS Applied Materials & Interfaces*, **2022**, *14*, 17889-17898. [Crossref], [Google Scholar], [Publisher]

[49]. P. Sun, Q. Gao, J. Liu, E. Liang, Q. Sun, Theoretical study of abnormal thermal expansion of cuscn and effect on electronic structure, *Frontiers in Materials*, **2021**, *8*, 712395. [Crossref], [Google Scholar], [Publisher]

[50]. C.H. Chang, M. Madasu, M.-H. Wu, P.-L. Hsieh, M.H. Huang, Formation of size-tunable CuI tetrahedra showing small band gap variation and high catalytic performance towards click reactions, *Journal of Colloid and Interface Science*, **2021**, *591*, 1-8. [Crossref], [Google Scholar], [Publisher]

[51]. R. Vettumperumal, J.R. Jemima, S. Kalyanaraman, R. Thangavel, Analysis of electronic and optical properties of copper iodide (γ-CuI) by TB–mBJ method–A promising optoelectronic material, *Vacuum*, **2019**, *162*, 156-162. [Crossref], [Google Scholar], [Publisher]

[52]. A. Thakur, D. Singh, S.K. Gill, Numerical simulations of 26.11% efficient planar CH3NH3PbI3 perovskite nip solar cell, *Materials Today: Proceedings*, **2022**, *71*, 195-201. [Crossref], [Google Scholar], [Publisher]

[53]. A. Roy, M. Benhaliliba, Investigation of ZnO/p-Si heterojunction solar cell: Showcasing experimental and simulation study, *Optik*, **2023**, *274*, 170557. [Crossref], [Google Scholar], [Publisher]

[54]. W. Wang, X. Li, L. Wen, Y. Zhao, H. Duan, B. Zhou, T. Shi, X. Zeng, N. Li, Y. Wang, Optical simulations of P3HT/Si nanowire array hybrid solar cells, *Nanoscale Research Letters*, **2014**, *9*, 1-6. [Crossref], [Google Scholar], [Publisher]

[55]. H. Higuchi, T. Negami, Largest highly efficient 203× 203 mm2 CH3NH3PbI3 perovskite solar modules, *Japanese Journal of Applied Physics*, **2018**, *57*, 08RE11. [Crossref], [Google Scholar], [Publisher]

[56]. X. Hu, Z. Huang, F. Li, M. Su, Z. Huang, Z. Zhao, Z. Cai, X. Yang, X. Meng, P. Li, Nacre-inspired crystallization and elastic “brick-and-mortar” structure for a wearable perovskite solar module, *Energy & Environmental Science*, **2019**, *12*, 979-987. [Crossref], [Google Scholar], [Publisher]

[57]. M. Alla, V. Manjunath, N. Chawki, D. Singh, S.C. Yadav, M. Rouchdi, F. Boubker, Optimized CH3NH3PbI3-XClX based perovskite solar cell with theoretical efficiency exceeding 30%, *Optical Materials*, **2022**, *124*, 112044. [Crossref], [Google Scholar], [Publisher]

[58]. F. Matebese, R. Taziwa, D. Mutukwa, Progress on the synthesis and application of CuSCN inorganic hole transport material in perovskite solar cells, *Materials*, **2018**, *11*, 2592. [Crossref], [Google Scholar], [Publisher]

[59]. Z. Tang, T. Bessho, F. Awai, T. Kinoshita, M.M. Maitani, R. Jono, T.N. Murakami, H. Wang, T. Kubo, S. Uchida, Hysteresis-free perovskite solar cells made of potassium-doped organometal halide perovskite, *Scientific reports*, **2017**, *7*, 12183. [Crossref], [Google Scholar], [Publisher]

[60]. T. Minemoto, Y. Kawano, T. Nishimura, J. Chantana, Numerical reproduction of a perovskite solar cell by device simulation

considering band gap grading, *Optical Materials*, **2019**, *92*, 60-66. [Crossref], [Google Scholar], [Publisher]

[61]. F. Fabregat-Santiago, G. Garcia-Belmonte, I. Mora-Seró, J. Bisquert, Characterization of nanostructured hybrid and organic solar cells by impedance spectroscopy, *Physical chemistry chemical physics*, **2011**, *13*, 9083-9118. [Crossref], [Google Scholar], [Publisher]

[62]. P. Afrin, K. Farjana, A. Vumije, M.N. Uddin, An investigation on the impact of temperature variation over the performance of formamidinium tin iodide perovskite solar cell using SCAPS simulation, *AIP Advances*, **2024**, *14*. [Crossref], [Google Scholar], [Publisher]

[63]. C.S. Guclu, Ş. Altındal, E.E. Tanrikulu, Voltage and frequency reliant interface traps and their lifetimes of the MPS structures interlayered with CdTe: PVA via the admittance method, *Physica B: Condensed Matter*, **2024**, *677*, 415703. [Crossref], [Google Scholar], [Publisher]

[64]. Z. Liu, Y. Lin, Testing trap states in polymer solar cells, *Polymer Testing*, **2024**, 108387. [Crossref], [Google Scholar], [Publisher]

[65]. A. Roy, A.K. Mukhopadhyay, M. Gupta, A. Majumdar, Negative capacitance effect of Cu–TiC thin film deposited by DC magnetron plasma, *Bulletin of Materials Science*, **2020**, *43*, 1-9. [Crossref], [Google Scholar], [Publisher]

[66]. A.S. Chouhan, N.P. Jasti, S. Avasthi, Effect of interface defect density on performance of perovskite solar cell: Correlation of simulation and experiment, *Materials Letters*, **2018**, *221*, 150-153. [Crossref], [Google Scholar], [Publisher]